

# Adaptive Image Enhancement for Tracing 3D Morphologies of Neurons and Brain Vasculatures

Zhi Zhou · Staci Sorensen · Hongkui Zeng ·  
Michael Hawrylycz · Hanchuan Peng

© Springer Science+Business Media New York 2014

**Abstract** It is important to digitally reconstruct the 3D morphology of neurons and brain vasculatures. A number of previous methods have been proposed to automate the reconstruction process. However, in many cases, noise and low signal contrast with respect to the image background still hamper our ability to use automation methods directly. Here, we propose an adaptive image enhancement method specifically designed to improve the signal-to-noise ratio of several types of individual neurons and brain vasculature images. Our method is based on detecting the salient features of fibrous structures, e.g. the axon and dendrites combined with adaptive estimation of the optimal context windows where such saliency would be detected. We tested this method for a range of brain image datasets and imaging modalities, including bright-field, confocal and multiphoton fluorescent images of neurons, and magnetic resonance angiograms. Applying our adaptive enhancement to these datasets led to improved accuracy and speed in automated tracing of complicated morphology of neurons and vasculatures.

**Keywords** Adaptive image enhancement · Anisotropic filtering · Gray-scale distance transformation · 3D neuron reconstruction · Vaa3D

## Introduction

Computational reconstruction of the 3D morphology of a neuron or a blood vessel from a microscopic image is important in many studies of brain science (Peng et al. 2013). For

---

Availability: This method has been implemented as an Open Source plugin for Vaa3D (<http://vaa3d.org>).

---

Z. Zhou · S. Sorensen · H. Zeng · M. Hawrylycz · H. Peng (✉)  
Allen Institute for Brain Science, Seattle, WA, USA  
e-mail: hanchuanp@alleninstitute.org

example, precise characterization of the neuron morphology can help profile the type and physiology of a neuron, e.g. (Kawaguchi et al. 2006; Krahe et al. 2011; DeFelipe et al. 2013). Despite its importance, manual reconstruction of these structures is extremely time-consuming and prone to error. To overcome many challenges in manual reconstruction, a number of previous studies have been done to automate the process of extracting the 3D morphology from 3D microscopic image stacks (Al-Kofahi et al. 2002; Choromanska et al. 2012; Cohen et al. 1994; Donohue and Ascoli 2011; Gillette et al. 2011; Lu et al. 2009; Peng et al. 2010a; Zhao et al. 2011; Xiao and Peng 2013).

However, one typical challenge in real world applications of such reconstructions is that the input image data may have a lot of noise and imperfect signals. This phenomenon is noteworthy in bright-field imaging of a biocytin labeled neuron (e.g. Fig. 1a), and it is also not uncommon in other types of biological and biomedical images, including confocal images of neurons and magnetic resonance images of blood vessels. Direct application of sophisticated automated neuron/vasculature reconstruction methods to an image with low signal-to-noise ratio (SNR) can yield poor results, such as many of the false branches in a 3D reconstruction in Fig. 1b.

Our goal in this article is to introduce a computational method to enhance the quality of an image that may contain one or more neurons or similar fibrous structures. As shown in the example in Fig. 1c, our method is able to increase the contrast of the image after the enhancement and at the same time preserve the key features of the fibrous structures in this image. With the processed image, the automated reconstruction can be done with improved accuracy and speed (Fig. 1d).

Image enhancement has been previously studied in many different ways, ranging from simple filtering in both frequency and spatial domains (Agaian et al. 2007; Greenspan et al. 2000) to more sophisticated processing based on anisotropy of the signal (Gerig et al. 1992; Weickert 1996; Yu and Acton

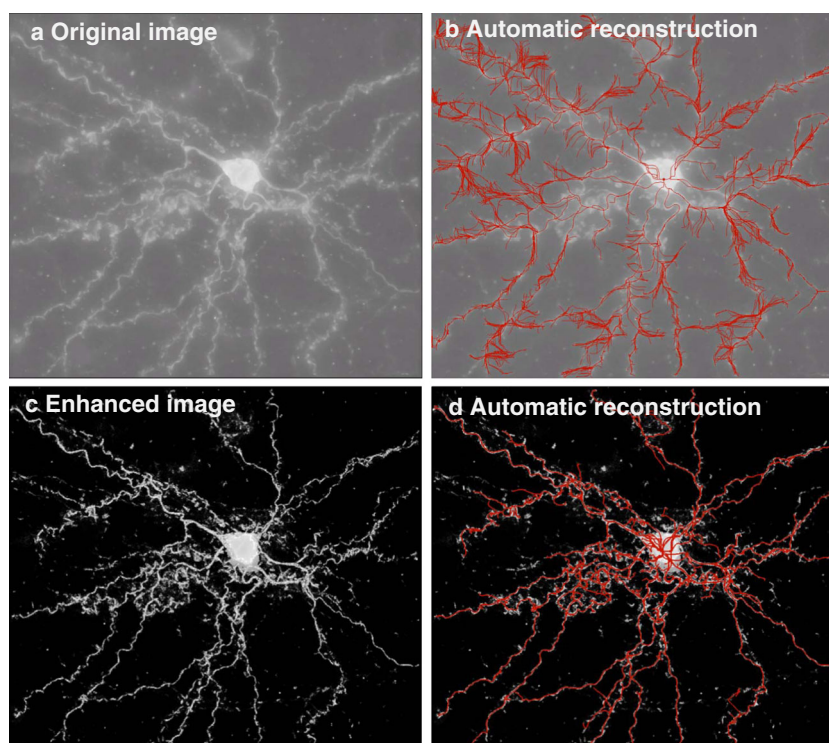


**Fig. 1** Maximum intensity projections of a bright-field image of a biocytin-labeled mouse neuron and the respectively enhanced image, along with reconstructions (*red*) produced for both images. The APP2 (all-path-pruning 2) method (Xiao and Peng 2013; Peng et al. 2011) was used for automated 3D reconstruction in this case. In **a**, the original image is a layer II/III pyramidal neuron with pixel resolution  $140 \text{ um} \times 140 \text{ um} \times 330 \text{ um}$ , imaged with a 60x, NA 1.42 objective, using an Olympus VS110 microscope system. In **b**, the automatic reconstruction result is generated

by APP2 method (18 s) based on the original image. In **c**, the enhanced image is obtained by our proposed adaptive enhancement approach with Gray-scale Distance Transformation (GSDT) information (Rutovitz 1968; Xiao and Peng 2013). In **d**, the automatic reconstruction result is generated by APP2 method (6 s) based on the enhanced image. Note that the soma is detected separately and merged with the enhanced neurite (see “Soma detection and fusion” section for the detail)

2002; Sato et al. 1997; Li et al. 2003). For images of neurons, or similar biomedical images that contain vessel-like tissues, many methods have been proposed (Hayman et al. 2004; Oberlaender et al. 2007). Our contributions in this study, however, are (1) a method specific for neuron and brain vasculature images, (2) an Open Source tool for related research, and (3) comprehensive testing of our method for a range of image datasets from different species and imaging modalities. We found that our method outperformed several previous approaches for our test data and produced high-SNR images that were suitable for automated reconstruction.

## Method

Without losing the generality, we present our method in the context of neuron reconstruction, which could also be used for brain vasculatures. A neuron consists of a cell body (soma) and a number of neurites, including the axon and dendrites. Depending on the efficiency of the neuron labeling based method, and the microscopy imaging system used, an acquired image stack may contain a substantial amount of noise and have high intensity background (Fig. 2a).

The purpose of our enhancement method is to detect the salient features of a neuron, its axon collaterals and dendrites, in a 3D image. Morphologically, the fiber-like axon and dendrites have strong anisotropy (Fig. 2a, zoomed-in views), hence we refined a method to explicitly quantify the anisotropy (see “Anisotropic filtering”) section to enhance the image. Since the calculated anisotropy value at any target image voxel location is also a function of the size of the window surrounding this voxel, it is important to estimate such local window size, or scale, adaptively. We formulated a way to estimate an adaptive scale for every voxel (Fig. 2b), which was then integrated into the method (see “GSDT based adaptive window size”) section.

## Anisotropic Filtering

As shown in Fig. 2, for any target location in the 3D image, we calculated a saliency score that indicates the anisotropy at that location. In a previous setting of 2D/3D line detection, the anisotropy can be computed using eigen-analysis of Hessian matrix of the target location (Li et al. 2003). In our case, for each voxel location  $(x,y,z)$ , we denoted the voxel intensity as

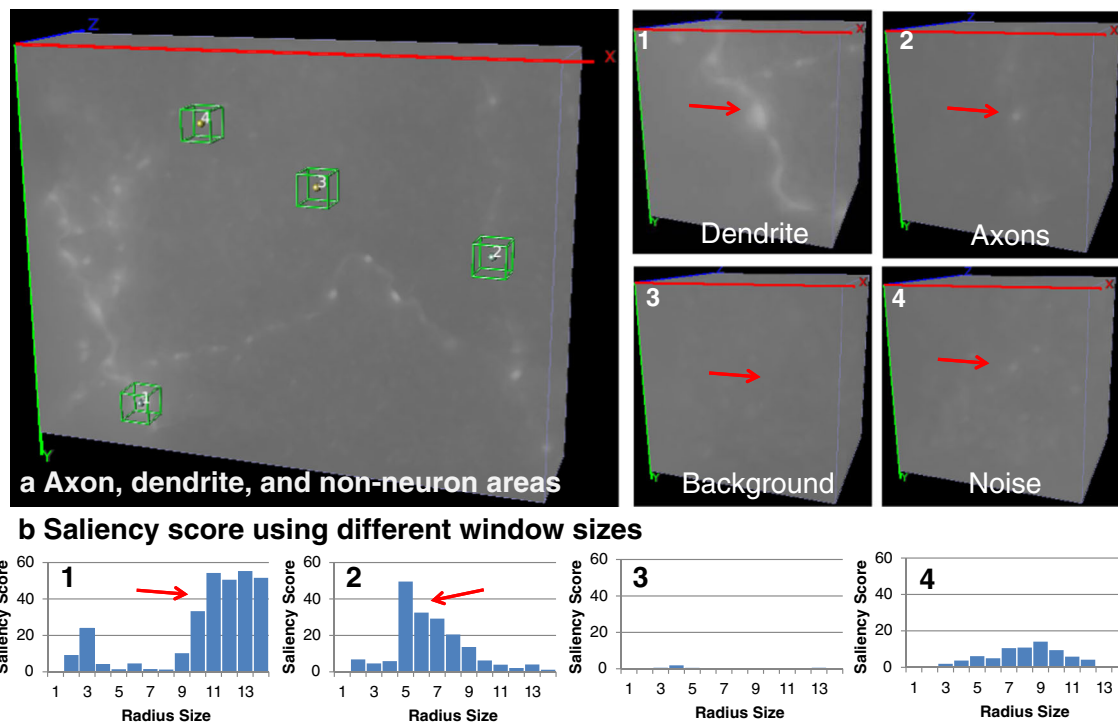


**Fig. 2** Salient feature analysis for neuron structures (axon and dendrite) and non-neuron image areas. In **a**, the zoomed-in view of four representative image areas (green boxes) are also shown. In **b**, the saliency score

(see Eq. 3) is calculated over a range of different window sizes. The red arrows show good radii of windows that are indicative in saliency detection

$f(x,y,z)$ . Thus based on a specific window size at this location, we calculated the Hessian matrix

$$H = \begin{bmatrix} f_{xx} & f_{xy} & f_{xz} \\ f_{yx} & f_{yy} & f_{yz} \\ f_{zx} & f_{zy} & f_{zz} \end{bmatrix},$$

where  $f_{ij}$  is the mixed second derivative along dimensions  $i$  and  $j$ . Since  $H$  is symmetric, i.e.  $f_{xy}=f_{yx}$ ,  $f_{xz}=f_{zx}$ , and  $f_{yz}=f_{zy}$ , the three eigenvalues  $\lambda_1$ ,  $\lambda_2$ , and  $\lambda_3$  of  $H$  exist. For convenience, we sort the eigenvalues based on their magnitude:  $|\lambda_1| \geq |\lambda_2| \geq |\lambda_3|$ .

In the method of (Li et al. 2003), an ideal 3D dot, line, and plane yield eigenvalues that satisfy the following conditions:

- Dot:  $\lambda_1 = \lambda_2 = \lambda_3 < 0$ ;
- Line:  $\lambda_1 = \lambda_2 < 0, \lambda_3 = 0$ ;
- Plane:  $\lambda_1 < 0, \lambda_2 = \lambda_3 = 0$ .

Clearly, for our case to detect the fiber-like or line-like structure, we should have a condition where  $\lambda_2$  and  $\lambda_3$  are as different as possible. Therefore, we defined a new magnitude function  $M(\lambda_1, \lambda_2, \lambda_3)$ ,

$$M(\lambda_1, \lambda_2, \lambda_3) = (|\lambda_2| - |\lambda_3|)^q, \tag{1}$$

and a new likelihood function  $L(\lambda_1, \lambda_2, \lambda_3)$ :

$$L(\lambda_1, \lambda_2, \lambda_3) = \frac{(|\lambda_2| - |\lambda_3|)}{|\lambda_1|}, \tag{2}$$

where  $q$  was chosen to be 2 in our experimental results.

In our setting, the magnitude and likelihood scores of the ideal 3D dot, line, and plane will be:

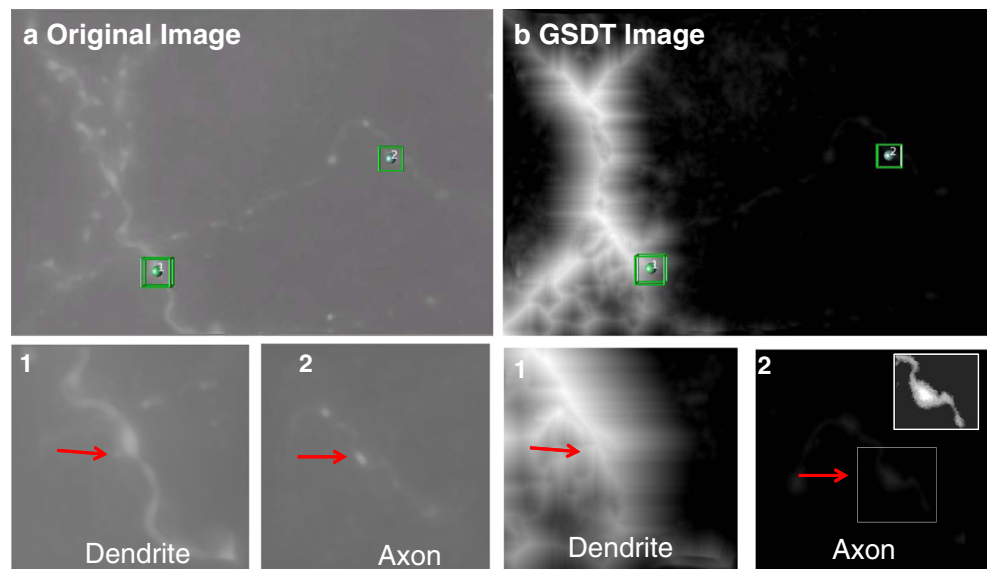
- Dot:  $M(\lambda_1, \lambda_2, \lambda_3) = 0, L(\lambda_1, \lambda_2, \lambda_3) = 0$ ;
- Line:  $M(\lambda_1, \lambda_2, \lambda_3) = (|\lambda_2|)^2, L(\lambda_1, \lambda_2, \lambda_3) = 1$ ;
- Plane:  $M(\lambda_1, \lambda_2, \lambda_3) = 0, L(\lambda_1, \lambda_2, \lambda_3) = 0$ .

In order to enhance 3D lines and suppress dot-like and plane-like structures in images, we thus designed the output  $O$  of the curvilinear enhancement filter as:

$$O(\lambda_1, \lambda_2, \lambda_3) = M(\lambda_1, \lambda_2, \lambda_3) \times L(\lambda_1, \lambda_2, \lambda_3) = \begin{cases} \frac{(|\lambda_2| - |\lambda_3|)^3}{|\lambda_1|} & \text{if } \lambda_1 < 0, \lambda_2 < 0 \\ 0 & \text{otherwise} \end{cases} \tag{3}$$

We calculated Eq. (3) using the eigenvalues  $\lambda_1, \lambda_2$ , and  $\lambda_3$  for every voxel in an image. Negative eigenvalues indicate that the intensity value of the target location is higher than its neighborhood. Since only bright objects surrounded by dark

**Fig. 3** Transform an original image to the GSDT image. In **a**, the zoomed-in view of two neuronal structures (*green boxes*) are shown in original image, which is a cropped area from a layer II/III pyramidal neuron with voxel resolution 140 um×140 um×330 um, imaged with a 60x, NA 1.42 objective, Olympus VS110 system. In **b**, the zoomed-in view of two neuronal structures (*green boxes*) show in GSDT image. In order to make the axon area to be more visible, we added another illumination-adjusted area in the top-right corner in B2



background should be enhanced, we consider only the voxel with negative eigenvalues as the signals. In addition, both the low intensity image background and high-frequency random noise will have relatively isotropic distribution of image voxel intensity around their locations, thus they can be filtered out using Eq. (3).

### GSDT Based Adaptive Window Size

The window size is important to estimate the meaningful Hessian matrix of a voxel. In Fig. 2b, we can see the window sizes that correspond to the high saliency scores for dendrites and axons are different. For relatively thick fibers, such as a

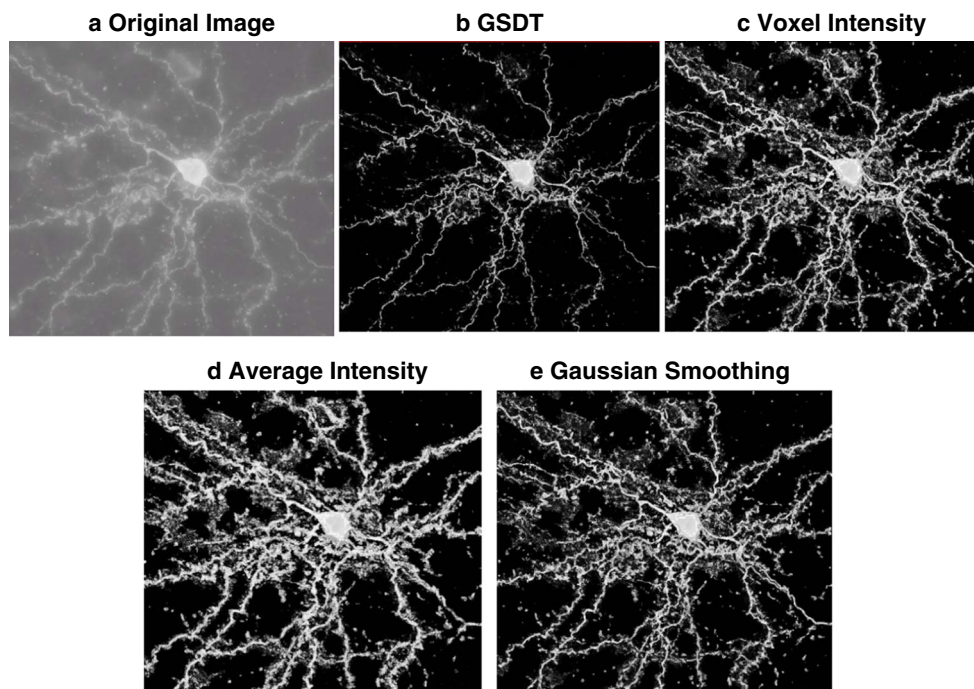


**Fig. 4** Enhancement comparison results using the window size based on different ways. In **b**, the windows size is based on GSDT value. In **c**, the window size is based on the voxel intensity value:  $S = \log_2 I(x, y, z)$ . In **d**, the window size is based on the average intensity of a 7\*7\*7 window surrounding each

voxel  $S = \log_2 \frac{1}{7*7*7} \sum_{i=-3}^3 \sum_{j=-3}^3 \sum_{k=-3}^3 I(x_i, y_j, z_k)$ . In **e**, the window size is based on the Gaussian smoothed (7\*7\*7 window size with  $\sigma=3$ ) voxel intensity  $S = \log_2 \frac{1}{7*7*7} \sum_{i=-3}^3 \sum_{j=-3}^3 \sum_{k=-3}^3 I(x_i, y_j, z_k) \times \text{Gaussian}(i, j, k)$

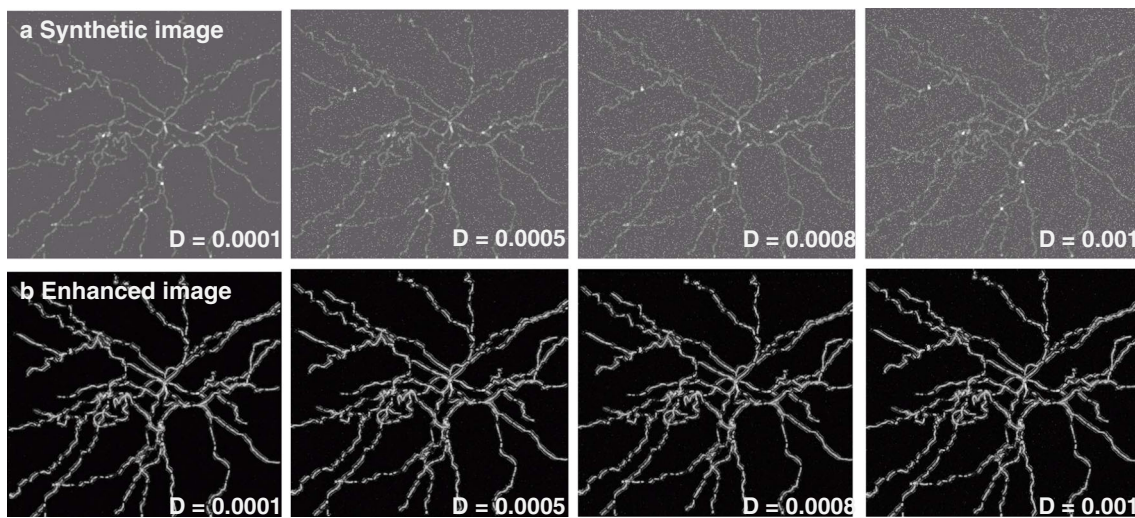


**Fig. 5** Enhancement results in four synthetic images. In **a**, there are four synthetic images with four different salt and pepper noise densities. In **b**, with the increasing of the noise density, the performance of our enhancement approach is very robust, and not sensitive to the noise level

dendrite, a window that is too small will use only the information of voxels inside the dendrite, which means that the pattern of consideration is actually isotropic and looks like a 3D dot-pattern. For thin fibers such as an axon, a window that is too large will make it hard to detect the curvilinear pattern using the Hessian analysis because the signal is often weak. On the other hand, Fig. 3a shows that the difference of signal intensity at two locations of a dendrite and an axon can be relatively small. This indicates that the intensity value alone may not be good enough to determine the window size.

Here we propose an approach using adaptive window sizes. First, we used the average image intensity as the threshold to

separate the image “foreground” from the “background”. Then, we ran the gray-scale distance transform (GSDT) (Rutovitz 1968; Xiao and Peng 2013) to find the voxel-intensity-aggregated shortest path for each foreground voxel. Different from the typical distance transform defined for a binary image, GSDT calculates the distance transform value of a pixel (voxel) to image background by summing up all gray-scale pixel values along the shortest path of the current pixel of consideration to the image background, and thus avoids image-thresholding that is often tricky to perform. GSDT can be implemented via the fast marching algorithm, which is essentially a breadth-first search over a graph where

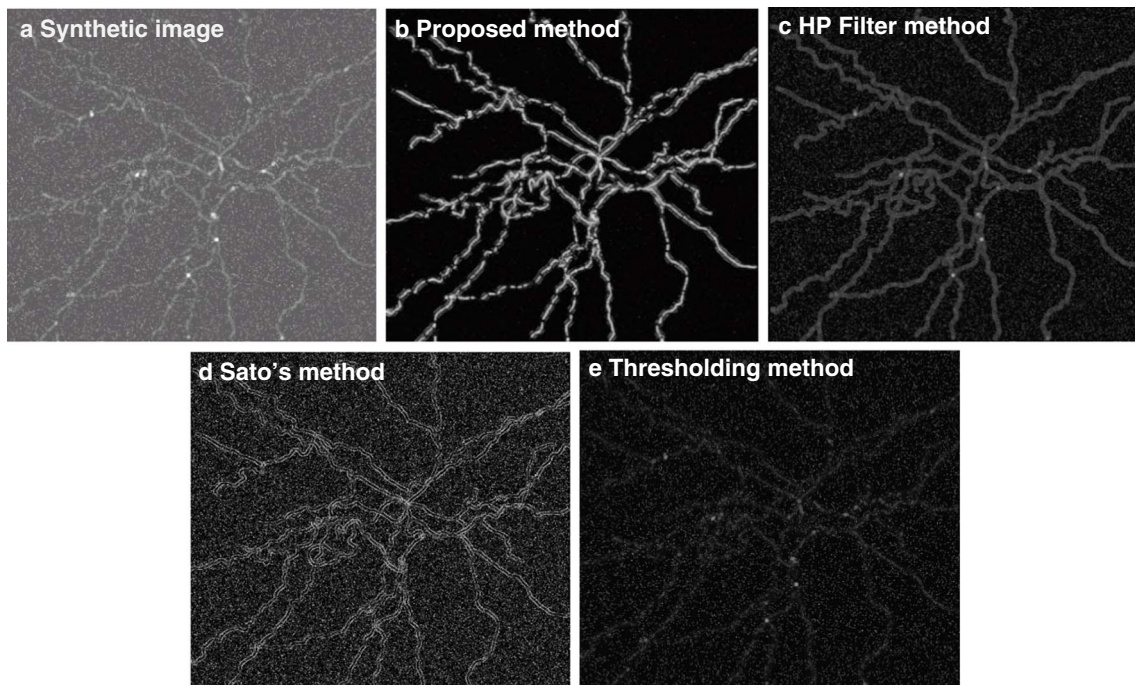


**Fig. 6** Comparison of enhancement results using the synthetic image (density=0.001). Four enhanced results for the synthesis image **a** are shown in **b-e**

each image voxel is represented as a graph node, and the graph edges are only defined for immediately adjacent image voxels. More detailed description of GSDT can be found in (Xiao and Peng 2013). After GSDT, the transformed image will have (a) bright intensity at the center curve of each foreground region, and (b) gradually decreasing intensity off the center of a foreground region.

Figure 3b shows a GSDT image from the original image (Fig. 3a). The intensity values of the dendrite and axon are similar in the original image, but the dendrite has much higher intensity value than the axons in the GSDT image. We took advantage of this useful information and defined an “optimal” window radius  $S$  for each voxel  $(x,y,z)$ :

$$S = \log_2 G(x,y,z), \quad (4)$$

where  $G(x,y,z)$  is the normalized (between 1 and 256) GSDT value for the location  $(x,y,z)$ , where the intensity normalization is done based on the highest GSDT value in the image. Indeed, in this way we basically used a window radius between 0 and 8. The actual window size, i.e. diameter, is defined as  $2*S+1$ . We have found Eq. (4) works well

empirically for all our testing data. For other data, a user may adjust Eq. (4) by multiplying a scaling factor. With this window size defined in this way, for each voxel we used Eq. (3) to calculate the Hessian matrix and then the enhanced output.

We also compared several alternative ways to compute the window size for adaptive image enhancement. Figure 4 shows the comparison results. It is shown that the enhancement image using GSDT value based window size (Fig. 4b) has a higher visual contrast than the images that are enhanced using voxel intensity based window size (Fig. 4c), average voxel intensity based window size (Fig. 4d), or Gaussian smoothed voxel intensity based window size (Fig. 4e).

### Multiscale Enhancement

Using the average image intensity as the background threshold, the GSDT image can predict the window size for bright-field images. However, the average image intensity may not provide a good threshold in some confocal (Figs. 8 and 13) and magnetic resonance angiography (MRA) images (Figs. 9

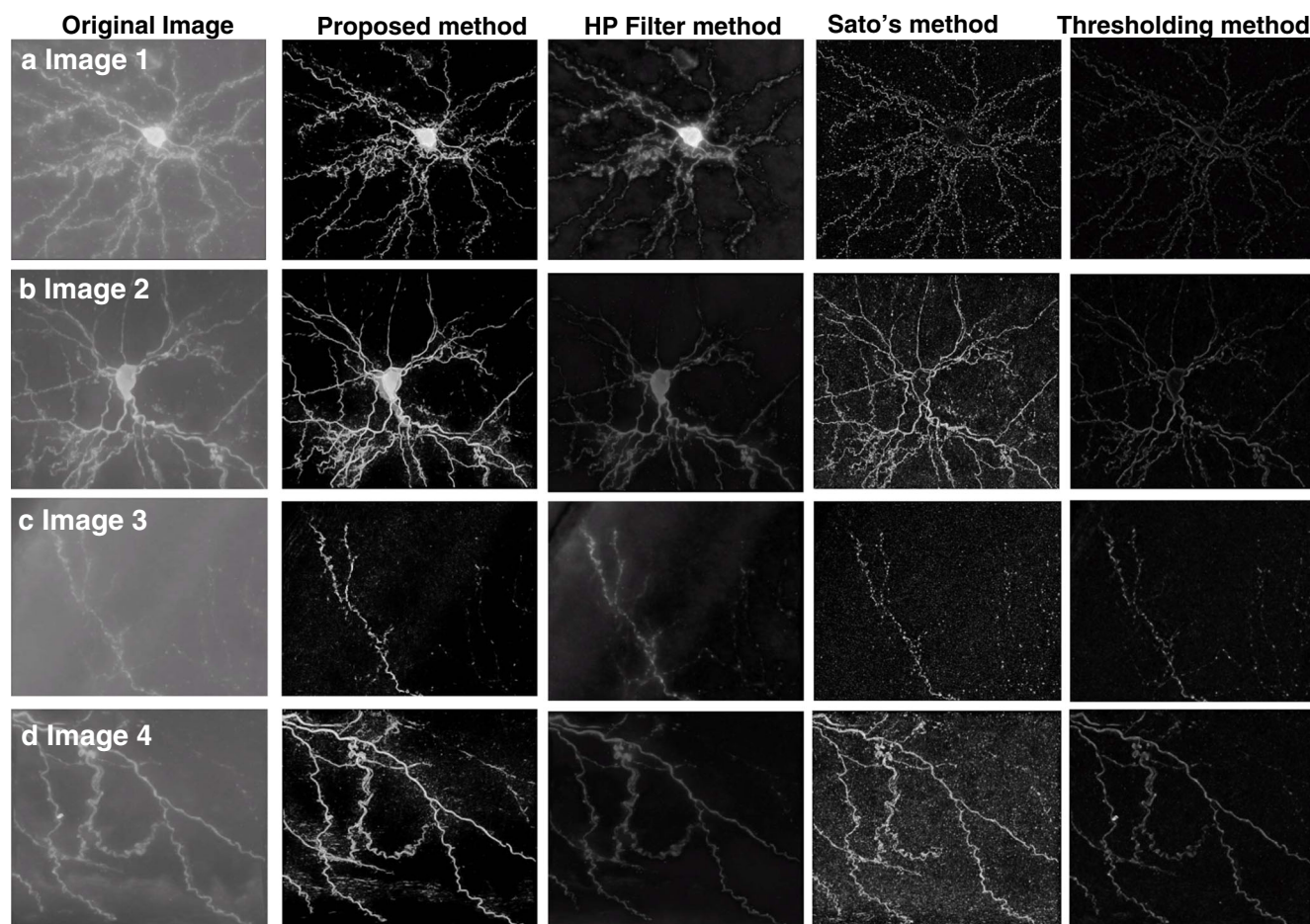


**Fig. 7** Enhancement comparison results in bright-field images. Original images in **a** and **c** are from one pyramidal neuron image, and original images in **b** and **d** are from another pyramidal neuron image. The

enhanced results for proposed method, HP filter method, Sato's method, and thresholding method are shown in **a-d** respectively

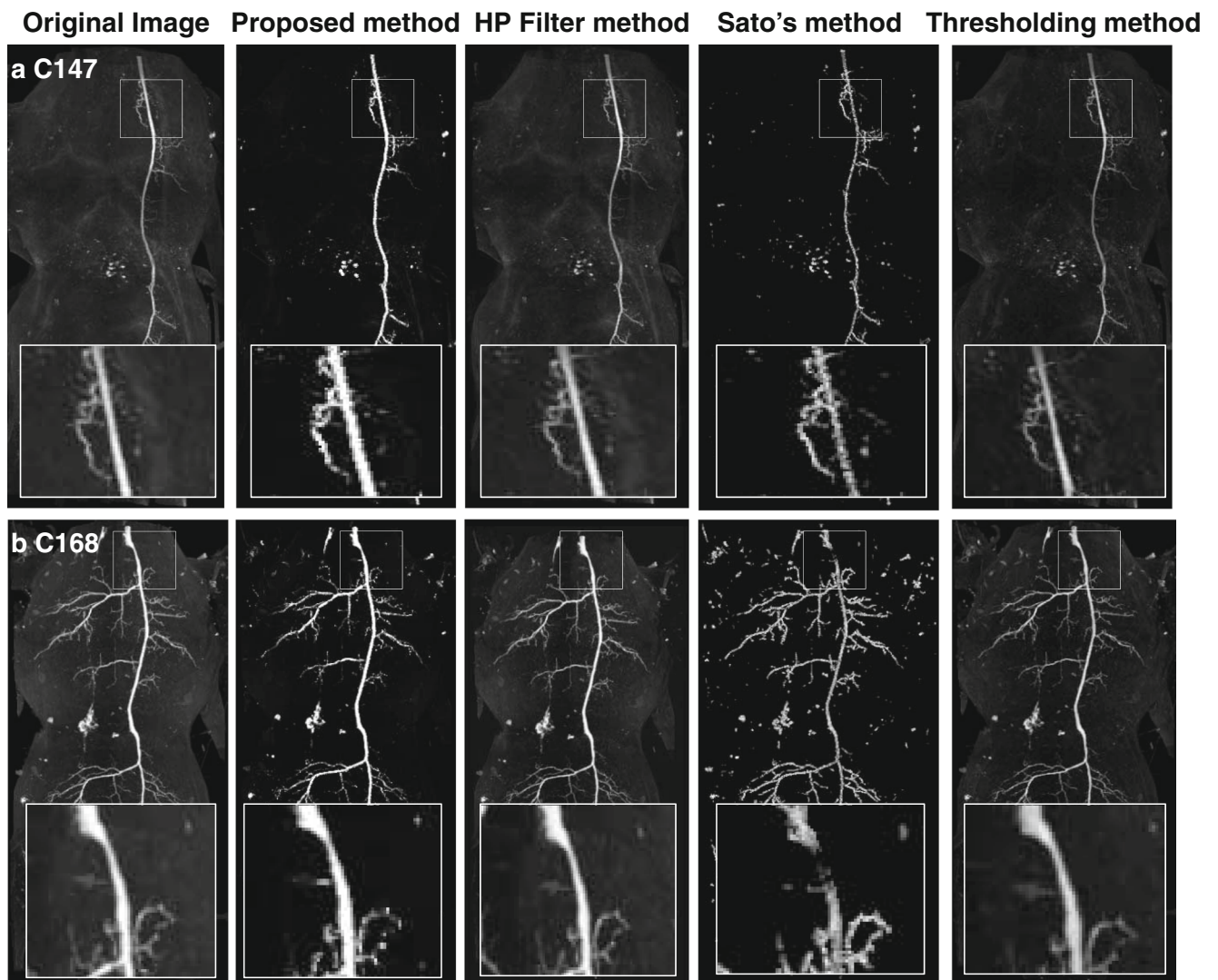


**Fig. 8** Enhancement comparison results for confocal images. In **a** and **b**, the zoomed-in view of neuronal areas are shown in the original and enhanced images

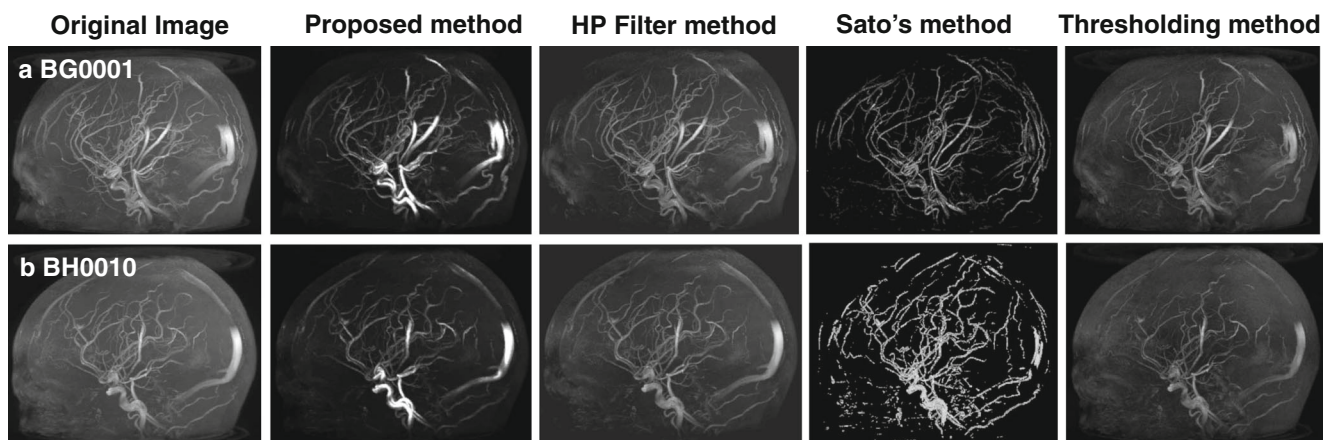


**Fig. 9** Enhancement comparison results in MRA brain images. The original image and four different enhanced images for the original image are shown in **a** and **b** respectively

**Table 1** The comparison of anisotropic evaluation scores in bright-field images

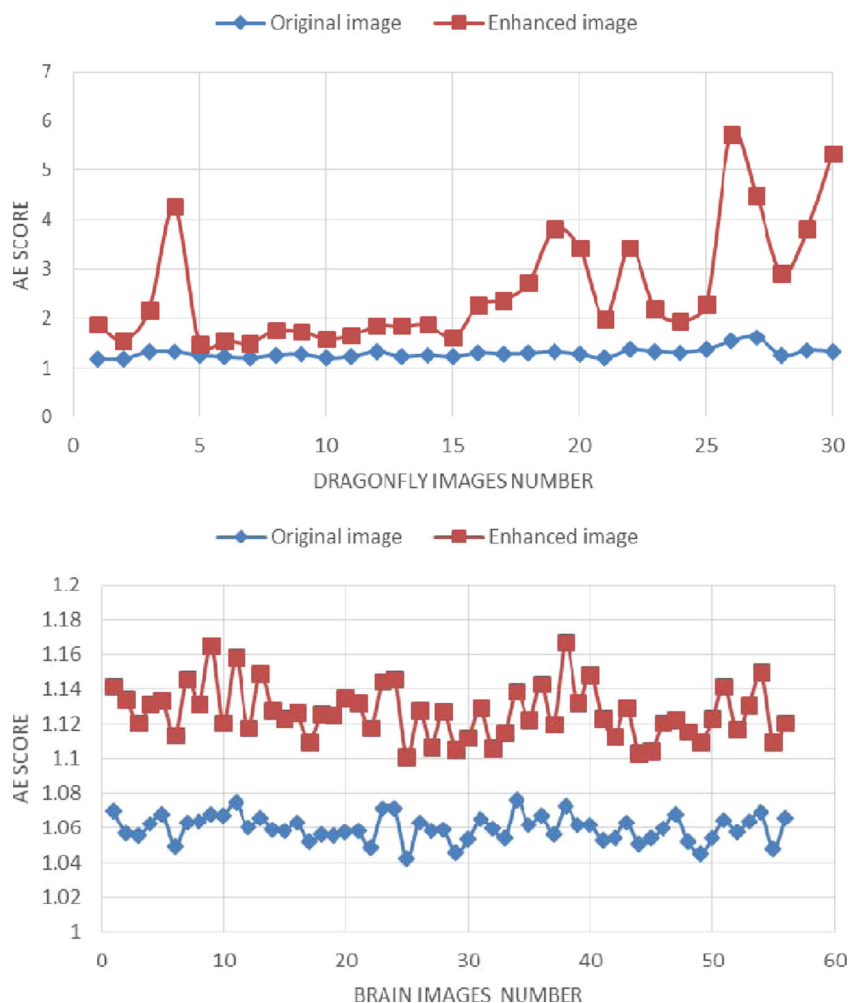
	Original image	Proposed method	HP filter method	Sato’s method	Thresholding method
Image 1	0.01	2.98	0.47	2.24	0.54
Image 2	0.23	2.19	0.42	2.07	0.23
Image 3	0.05	1.09	0.59	1.05	0.23
Image 4	0.05	1.72	0.51	1.46	0.08

and14). In the situation of highly uneven background, the GSDT image cannot provide useful information to determine the window size. In such a case, in addition to using adaptive window size for a single scale, we also used a multiscale approach.

Similar to the method used in (Li et al. 2003), for each scale  $k$ , we smoothed the image by Gaussian filter with a standard deviation  $\sigma_k$ . After that, we calculated the saliency score  $I_k$  with fixed window size using Eq. (3) on the smoothed image. The final enhanced output  $O$  for each voxel is obtained using:

$$O = \max(\sigma_k^2 \times I_k), k = 2, 3, \dots \tag{5}$$

**Fig. 10** The comparison of anisotropic evaluation scores in confocal and MRA images. The AE score for original image is red, and the AE score for enhanced image is blue



Since the extra-thin signal (with 1 voxel width) could be smoothed out by Gaussian filter, we only considered  $k$  values greater than 1. The number of scales was chosen to be 3 in our experimental results.

Soma Detection and Fusion

Since our proposed approach is designed to enhance only line-like structures, the soma of a neuron (e.g. Fig. 7a and b) will be eliminated. In order to enhance the image with the soma completely, we designed the following approach to detect the cell body. We first followed the soma detection in (Xiao and Peng 2013) by applying GSDT to the image and found the

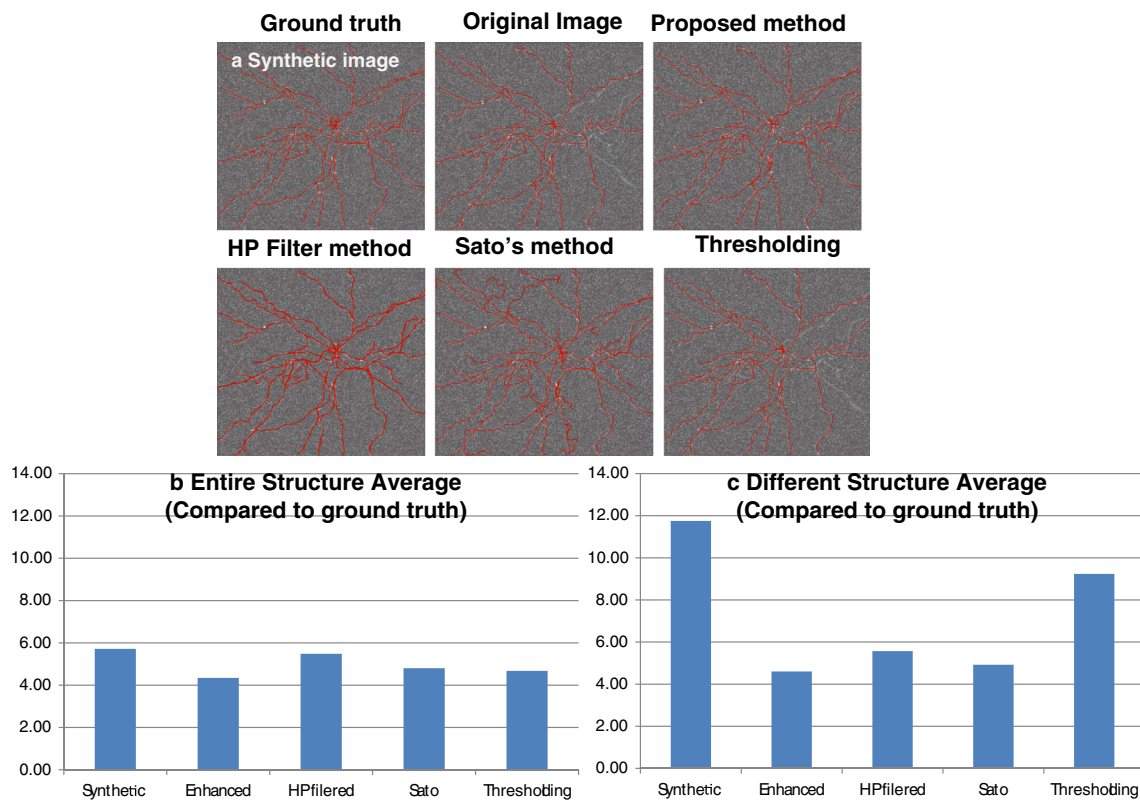


**Fig. 11** Reconstruction comparison results using the synthetic image (density=0.001). For better visualization, the reconstructions are overlaid on top of the original images for different enhanced images in **a**. Two

reconstruction distance scores to the ground truth for these four enhanced images are shown in **b** and **c**

centers of candidate cell bodies that correspond to local maxima of the GSDT image. Based on each of these centers, we recalculated a GSDT value for the local soma-centered area with higher background threshold (we used the average intensity  $\mu+3 * \text{variance } \sigma$  in this case). The final enhanced image with the soma is fused by:

$$O_{fused}(x) = \begin{cases} I(x) & G(x) > T_{gsdt} \\ O(x) & else \end{cases}, \tag{6}$$

where  $x$  is a voxel,  $I(x)$  is the intensity value,  $G(x)$  is the local GSDT value for  $x$ ,  $T_{gsdt}$  is the threshold to determine if the voxel is within the soma area or not, and  $O(x)$  is the enhanced result before soma detection. Based on Eq. (6), if the local GSDT value is higher than the threshold, we assumed it is a soma voxel. Thus we copied the original intensity value to the final enhance result. Otherwise we kept the original enhanced result.

### Experimental Results

We used synthetic images, bright-field images, confocal images, and MRA images to test our proposed enhancement approach. For the comparison, we also used three methods:

a high pass (HP) filter method, Sato’s enhancement method (Sato et al. 1997), and an adaptive thresholding method (using the average intensity of each voxel’s neighbors as the adaptive threshold).

#### Our Enhancement Method Can Better Preserve Signals, Remove Noise, and Suppress Background

In the first experiment, we generated synthetic images that have different noise levels. We began with generating an image that contains a few neuron structures (0 for background, and 255 for signals). Then we applied a Gaussian smooth filter to it, followed by adding high intensity background to make the image has a similar appearance to a bright-field image. Finally, we added salt and pepper noise (a common type of noise in microscopic images) (Andersen and Kak 1984) with different densities to synthesize a set of images.

Figure 5a shows the four synthetic images with noise density 0.0001, 0.0005, 0.0008, and 0.001. Noise density  $D$  means  $D*(\text{total number of voxels})$  will be affected. Higher noise density indicates a lower SNR of an image. Figure 5b shows the enhancement results for these four synthetic images correspondingly. Figure 5 clearly shows that our method enhances the signal and depresses the background and noise very well.

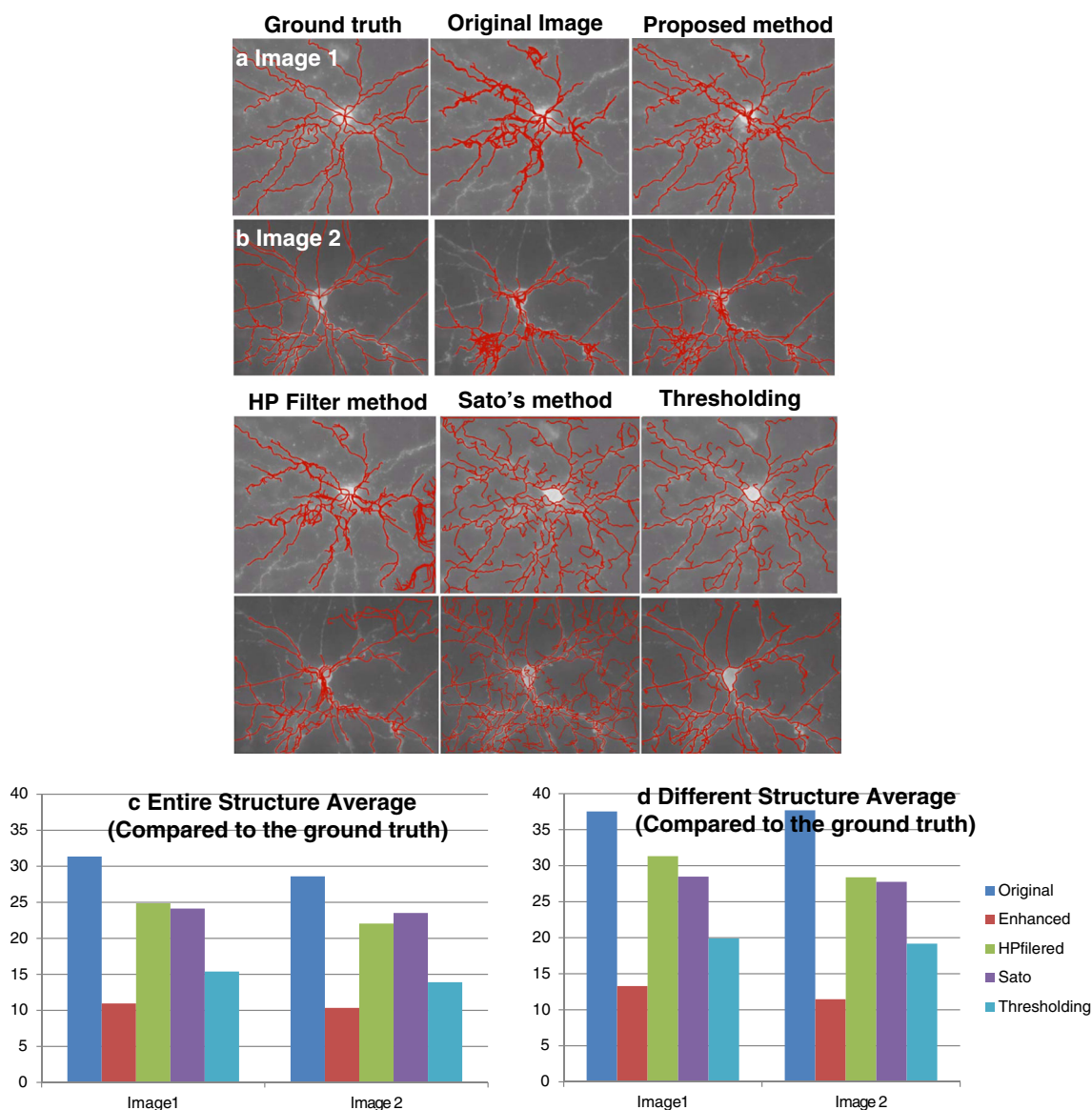
Figure 6 shows the enhancement comparison results for the synthetic image with noise density 0.001. Compared to the HP filtered image (Fig. 6c), Sato's enhanced image (Fig. 6d), and thresholded image (Fig. 6e), our enhanced image (Fig. 6b) has much better contrast and less noise.

Figure 7 shows the comparison of enhancement results for bright-field images. These four images are the cropped areas from layer II/III single pyramidal neuron images. For all four images, our enhancement produced more meaningful results than the others. Particularly, as shown in Figure 7b, our enhanced image has captured and enhanced both dendrites and axons while other approaches failed.

We tested 30 confocal images of dragonfly neurons which have smaller scales and better SNR (Gonzalez-Bellido et al. 2013). As we discussed in 2.3, the multiscale approach is

used. Figure 8 shows a comparison of the enhancement results of two confocal images (C147, and C168). In Figure 8a and b, it is shown that our proposed method provides better-enhanced signals than HP filter and thresholding methods. Moreover, compared to Sato's method, signals in our enhanced images are more continuous.

We also evaluated our enhancement approach using 56 MRA brain images (Wright et al. 2013; The Brain Vasculature (BraVa 2014) database). Similar to the experiment setting we have on confocal images, the multiscale approach is used for the enhancement. Figure 9 shows the enhancement comparison results of two MRA images (BG0001 and BH0010). Our enhanced images can suppress noise and enhance images similar to the case of bright-field and confocal images.



**Fig. 12** Reconstruction comparison results for bright-field images. For better visualization, the reconstructions are overlaid on top of the original images for different enhanced images in **a** and **b**. The color schemes in **c** and **d** are the same

Anisotropic Evaluation Measurement Quantitatively Indicates Enhanced Curvilinear Structures in Images

To quantitatively evaluate the image enhancement, we used the Anisotropic Evaluation (AE) score as the criterion. AE is defined as:

$$AE = \frac{1}{K_x K_y K_z} \sum_{x=1}^{K_x} \sum_{y=1}^{K_y} \sum_{z=1}^{K_z} \left( E_{max}(x, y, z) / E_{2nd}(x, y, z) \right), \quad (7)$$

where  $K_x$ ,  $K_y$ , and  $K_z$  are the x, y, z dimensions of the image.  $E_{max}(x, y, z)$  and  $E_{2nd}(x, y, z)$  are the greatest and the second greatest eigenvalues of the covariance matrix of a surrounding window of voxel  $(x, y, z)$  where the mean intensity has been subtracted. Eq. (7) provides a different way from Eq. (3) to assess the spatial anisotropy. A high AE score indicates a high contrast and good enhancement of the image. Some other enhancement measurements (e.g. principal component analysis, contrast)

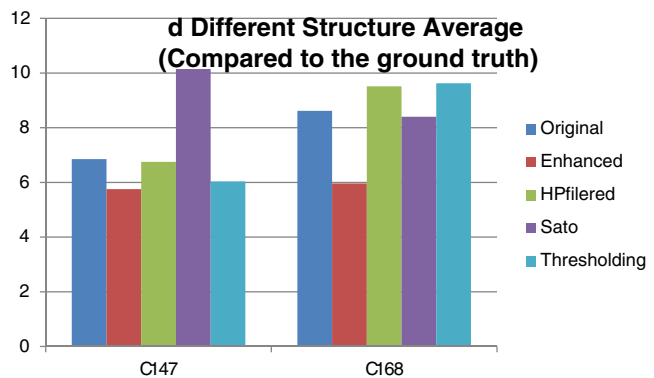
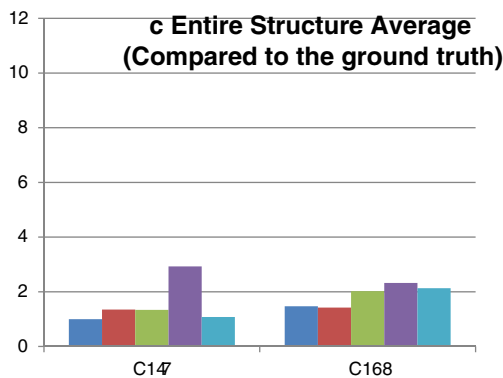
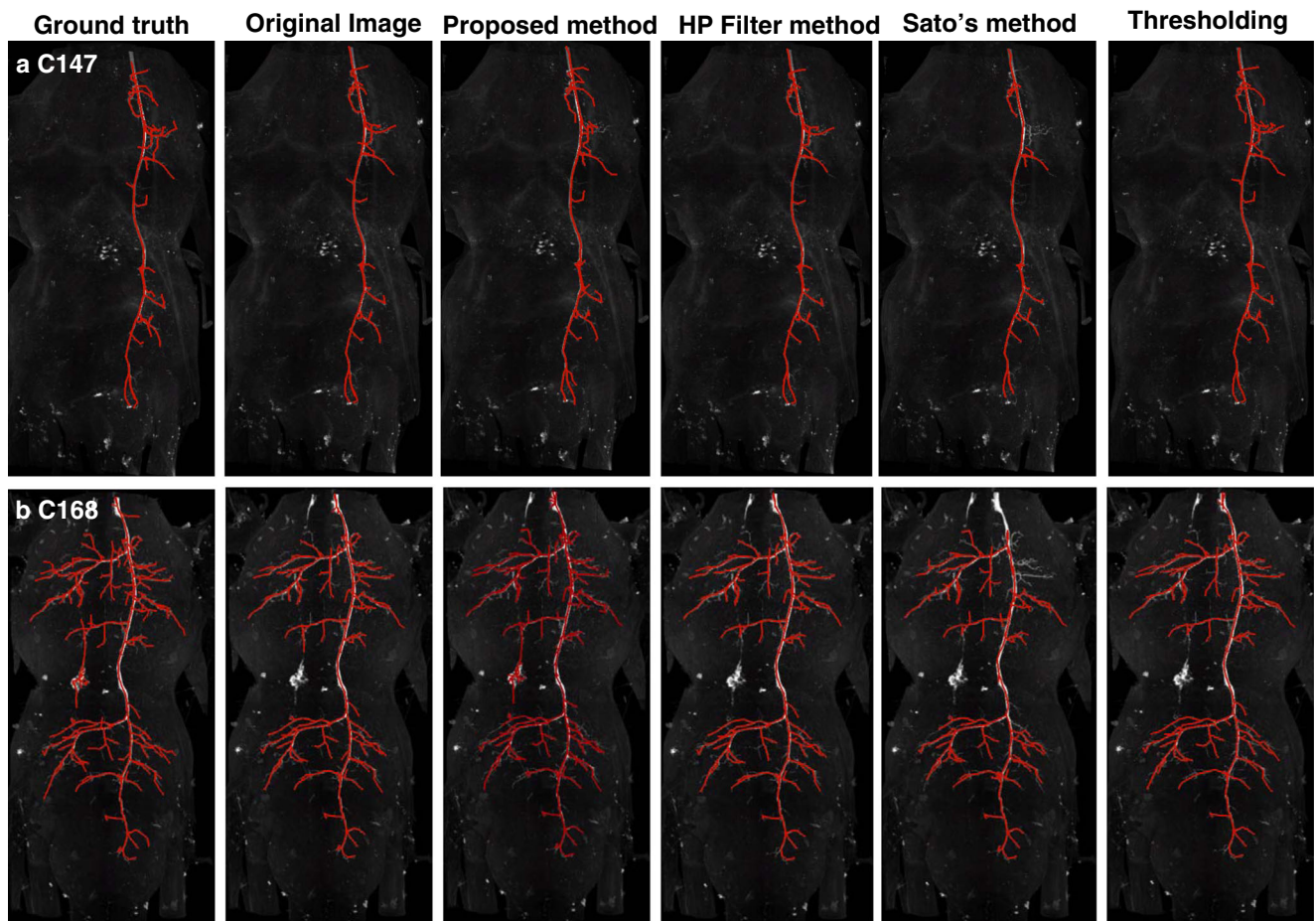


Fig. 13 Reconstruction comparison results for confocal dragonfly images. For better visualization, the reconstructions are overlaid on top of the original images for different enhanced images in a and b. The color schemes in c and d are the same

could also be used to evaluate the enhancement performance.

Table 1 shows the AE scores of bright-field images. Our enhanced image has obviously higher AE score than other methods.

Figure 10 shows the AE scores for confocal images (Figure 10a) and MRA images (Figure 10b). Our enhanced images have higher AE scores than the original images, indicating that our proposed method can better represent the anisotropic properties of neurons and brain vasculatures.

#### Vessel-Like Structures in Neurons and Brain Vasculatures Can Be Better Reconstructed Using Our Enhanced Image

In order to check if our enhanced image can improve the automatic tracing, we considered using some automated neuron tracing to help the evaluation. Here, as an example, we used the all-path-pruning 2.0 (APP2) method (Xiao and Peng 2013; Peng et al. 2011), which was previously shown to be able to extract neuron morphology reliably for many confocal images. Since different parameters in APP2 could generate different reconstruction results, to be fair, we always used the best results for comparison.

To check whether or not the enhanced image would be good for neuron and vasculature reconstructions, we also

compared the automatically generated reconstructions with manually produced reconstructions.

We used two spatial distance scores used in previous studies (Peng et al. 2010a) to assess the similarity of differently produced reconstructions for the same neuron. The first score (“entire structure average”) measures the average shortest distance between two reconstructions’ compartments. The second score (“different structure average”) measures the average distance between corresponding compartments that are apart from each other with a visible spatial separation (defined  $\geq 2$  voxels apart).

Figure 11 shows the reconstruction comparison result using the synthetic image. It can be seen that the reconstruction using our enhanced image has smaller distances to the ground truth compared to several other enhancement methods.

Figure 12 shows the comparison of reconstruction results for bright-field images. To conduct this experiment, we chose two areas from these bright-field images, i.e., Figure 8a and b, and manually traced them as the ground truth. Taking the ground truth as the reference, the reconstruction based on our enhanced images is much better than that based on original images, HP filtered images, Sato’s enhanced images, and thresholded images. To quantitatively evaluate the performance, we also calculated two distance scores (Fig. 12c and d) between these five reconstructions and the ground truth. The distances between the reconstruction using our

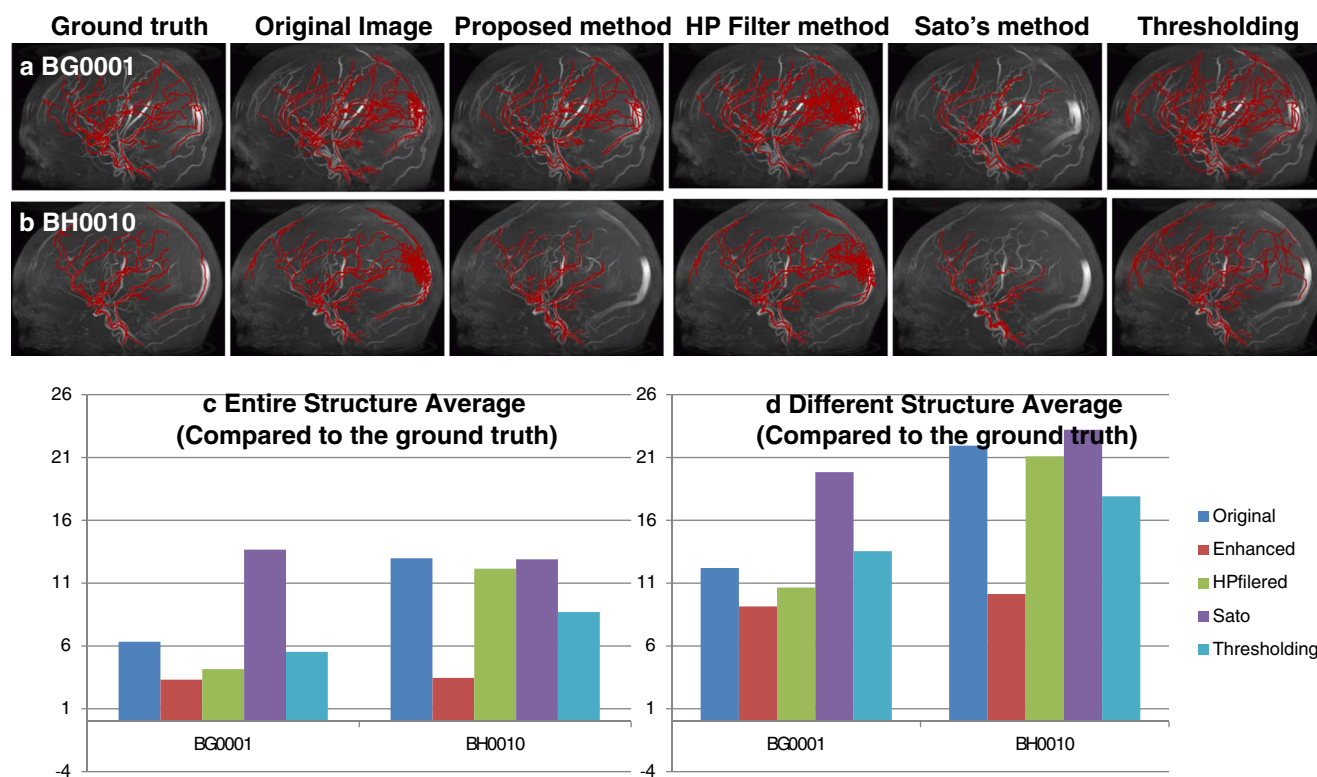


**Fig. 14** Reconstruction comparison results in MRA brain images. For better visualization, the reconstructions are overlaid on top of the original images for different enhanced images in **a** and **b**. The color schemes in **c** and **d** are the same

enhancement and the ground truth are much smaller compared to others. This result indicates that our image enhancement method provides an improved input for automated tracing.

Figure 13 shows the reconstruction comparison results for two confocal images (C147, and C168). With several predefined markers, APP2 approach has been tested to be the most accurate automatic tracing method in these confocal dragonfly images. Thus we used the APP2 reconstruction with markers as the ground truth. For reconstruction (Fig. 13c), the entire structure average distance for the enhanced image is comparable to others. In Fig. 13d, the different structure average distances for our enhanced image are lower than that of other images.

Figure 14 shows the reconstruction comparison results in MRA brain images. It is shown that the reconstruction results from our enhanced image have better performance and lower distance to the human manual reconstruction results.

In our experiments, we used a Linux machine with Intel(R) Xeon(R) 3.60GHz CPU. Our enhancement method was implemented in C++ as a plugin program on the Vaa3D platform (Peng et al. 2010b; Peng et al. 2014). Our method took 16 minutes to enhance a bright-field mouse neuron image with  $1,369 \times 1,073 \times 133$  voxels, and about 60 seconds to enhance both a confocal dragonfly neuron image ( $261 \times 512 \times 174$  voxels) and a MRA brain image ( $288 \times 320 \times 199$  voxels).

## Conclusion and Discussion

In this paper, we proposed an adaptive image enhancement method to improve the signal-to-noise ratio of images. We designed an anisotropic filtering based approach to detect the salient features and suppress background and high frequency noise. Based on the type of images, we used GSDT based adaptive window size, or a multiscale approach to detect signals in different scales. We have compared our new method to three other methods on a range of brain image datasets. Our enhanced images have higher anisotropic scores and facilitate automatic tracing for more accurate results. It is also shown that 3D morphologies of neurons and brain vasculatures can be more accurately and efficiently reconstructed using our adaptive enhancement method.

Of note, our method has been designed for enhancing light microscopy images and similar data. For interesting electron-microscopy datasets used in neuroscience, e.g. (Kim et al. 2014; Helmstaedter et al. 2013), our method has limitation as the local image patches extracted from such dense images will not exhibit similar anisotropy, unless specially designed image filters are first used to remove small fragments followed by applying our method. This can be an interesting future direction of research.

## Information Sharing Statement

All codes for our adaptive image enhancement are available in open source and can be found on Vaa3D (RRID:nlx\_156012) source code repository ([https://svn.janelia.org/penglab/projects/vaa3d\\_tools/released\\_plugins/v3d\\_plugins/multiscaleEnhancement/](https://svn.janelia.org/penglab/projects/vaa3d_tools/released_plugins/v3d_plugins/multiscaleEnhancement/)).

**Acknowledgments** We thank Rafael Yuste for providing samples of mouse pyramidal neurons, Paloma Gonzalez-Bellido for providing the dragonfly confocal images, Peter Kochunov for providing the MRA brain images, and Brian Long for comments. This work is supported by Allen Institute for Brain Science.

## References

- Agaian, S. S., Silver, B., & Panetta, K. A. (2007). Transform coefficient histogram-based image enhancement algorithms using contrast entropy. *Image Processing, IEEE Transactions on*, 16(3), 741–758.
- Al-Kofahi, K. A., Lasek, S., Szarowski, D. H., Pace, C. J., Nagy, G., Turner, J. N., & Roysam, B. (2002). Rapid automated three-dimensional tracing of neurons from confocal image stacks. *Information Technology in Biomedicine, IEEE Transactions on*, 6(2), 171–187.
- Andersen, A., & Kak, A. (1984). Simultaneous algebraic reconstruction technique (SART): a superior implementation of the ART algorithm. *Ultrasonic Imaging*, 6(1), 81–94.
- Choromanska, A., Chang, S.-F., & Yuste, R. (2012). Automatic reconstruction of neural morphologies with multi-scale tracking. *Frontiers in neural circuits*, 6.
- Cohen, A., Roysam, B., & Turner, J. (1994). Automated tracing and volume measurements of neurons from 3-D confocal fluorescence microscopy data. *Journal of Microscopy*, 173(2), 103–114.
- DeFelipe J, López-Cruz PL, Benavides-Piccione R, Bielza C, Larrañaga P, Anderson S, Burkhalter A, Cauli B, Fairén A, Feldmeyer D (2013) New insights into the classification and nomenclature of cortical GABAergic interneurons. *Nature Reviews Neuroscience*
- Donohue, D. E., & Ascoli, G. A. (2011). Automated reconstruction of neuronal morphology: an overview. *Brain Research Reviews*, 67(1), 94–102.
- Gerig, G., Kubler, O., Kikinis, R., & Jolesz, F. A. (1992). Nonlinear anisotropic filtering of MRI data. *Medical Imaging, IEEE Transactions on*, 11(2), 221–232.
- Gillette, T. A., Brown, K. M., Svoboda, K., Liu, Y., & Ascoli, G. A. (2011). DIADEMchallenge. Org: a compendium of resources fostering the continuous development of automated neuronal reconstruction. *Neuroinformatics*, 9(2), 303–304.
- Gonzalez-Bellido, P. T., Peng, H., Yang, J., Georgopoulos, A. P., & Olberg, R. M. (2013). Eight pairs of descending visual neurons in the dragonfly give wing motor centers accurate population vector of prey direction. *Proceedings of the National Academy of Sciences*, 110(2), 696–701.
- Greenspan, H., Anderson, C. H., & Akber, S. (2000). Image enhancement by nonlinear extrapolation in frequency space. *Image Processing, IEEE Transactions on*, 9(6), 1035–1048.
- Hayman, M., Smith, K., Cameron, N., & Przyborski, S. (2004). Enhanced neurite outgrowth by human neurons grown on solid three-dimensional scaffolds. *Biochemical and Biophysical Research Communications*, 314(2), 483–488.
- Helmstaedter, M., Briggman, K. L., Turaga, S. C., Jain, V., Seung, H. S., & Denk, W. (2013). Connectomic reconstruction of the inner plexiform layer in the mouse retina. *Nature*, 500(7461), 168–174.

- Kawaguchi, Y., Karube, F., & Kubota, Y. (2006). Dendritic branch typing and spine expression patterns in cortical nonpyramidal cells. *Cerebral Cortex*, *16*(5), 696–711.
- Kim, J. S., Greene, M. J., Zlateski, A., Lee, K., Richardson, M., Turaga, S. C., Purcaro, M., Balkam, M., Robinson, A., & Behabadi, B. F. (2014). Space-time wiring specificity supports direction selectivity in the retina. *Nature*, *509*(7500), 331–336.
- Krahe, T. E., El-Danaf, R. N., Dilger, E. K., Henderson, S. C., & Guido, W. (2011). Morphologically distinct classes of relay cells exhibit regional preferences in the dorsal lateral geniculate nucleus of the mouse. *The Journal of Neuroscience*, *31*(48), 17437–17448.
- Li, Q., Sone, S., & Doi, K. (2003). Selective enhancement filters for nodules, vessels, and airway walls in two-and three-dimensional CT scans. *Medical Physics*, *30*, 2040.
- Lu, J., Fiala, J. C., & Lichtman, J. W. (2009). Semi-automated reconstruction of neural processes from large numbers of fluorescence images. *PLoS One*, *4*(5), e5655.
- Oberlaender, M., Bruno, R. M., Sakmann, B., & Broser, P. J. (2007). Transmitted light brightfield mosaic microscopy for three-dimensional tracing of single neuron morphology. *Journal of Biomedical Optics*, *12*(6), 064029.
- Peng, H., Ruan, Z., Atasoy, D., & Sternson, S. (2010a). Automatic reconstruction of 3D neuron structures using a graph-augmented deformable model. *Bioinformatics*, *26*(12), i38–i46.
- Peng, H., Ruan, Z., Long, F., Simpson, J. H., & Myers, E. W. (2010b). V3D enables real-time 3D visualization and quantitative analysis of large-scale biological image data sets. *Nature Biotechnology*, *28*(4), 348–353.
- Peng, H., Long, F., & Myers, G. (2011). Automatic 3D neuron tracing using all-path pruning. *Bioinformatics*, *27*(13), i239–i247.
- Peng, H., Roysam, B., & Ascoli, G. A. (2013). Automated image computing reshapes computational neuroscience. *BMC Bioinformatics*, *14*(1), 293.
- Peng, H., Bria, A., Zhou, Z., Iannello, G., & Long, F. (2014). Extensible visualization and analysis for multidimensional images using Vaa3D. *Nature Protocols*, *9*(1), 193–208.
- Rutovitz D (1968) Data structures for operations on digital images. Pictorial pattern recognition:105–133
- Sato Y, Nakajima S, Atsumi H, Koller T, Gerig G, Yoshida S, Kikinis R 3D multi-scale line filter for segmentation and visualization of curvilinear structures in medical images. In: CVRMed-MRCAS'97, 1997. Springer, pp 213–222
- The Brain Vasculature (BraVa) database (2014). The Krasnow Institute for Advanced Study, George Mason University. <http://cng.gmu.edu/brava>.
- Weickert J (1996) Theoretical foundations of anisotropic diffusion in image processing. In: Theoretical foundations of computer vision. Springer, pp 221–236
- Wright SN, Kochunov P, Mut F, Bergamino M, Brown KM, Mazziotta JC, Toga AW, Cebal JR, Ascoli GA (2013) Digital Reconstruction and Morphometric Analysis of Human Brain Arterial Vasculature from Magnetic Resonance Angiography. NeuroImage
- Xiao, H., & Peng, H. (2013). APP2: automatic tracing of 3D neuron morphology based on hierarchical pruning of a gray-weighted image distance-tree. *Bioinformatics*, *29*(11), 1448–1454.
- Yu, Y., & Acton, S. T. (2002). Speckle reducing anisotropic diffusion. *Image Processing, IEEE Transactions on*, *11*(11), 1260–1270.
- Zhao, T., Xie, J., Amat, F., Clack, N., Ahammad, P., Peng, H., Long, F., & Myers, E. (2011). Automated reconstruction of neuronal morphology based on local geometrical and global structural models. *Neuroinformatics*, *9*(2–3), 247–261.